Engineering multiphasic MoSe₂/NiSe heterostructure interfaces for superior hydrogen production electrocatalysis

Jiang-Yan Xue [a,b], Fei-Long Li [c,*], Bingbing Chen [d], Hongbo Geng [c,*], Wei Zhang [a], Wan-Ying Xu [a], Hongwei Gu [a], Pierre Braunstein [e], Jian-Ping Lang [a,b,**]

[a] *College of Chemistry, Chemical Engineering and Materials, Soochow University, Suzhou 215123, Jiangsu, People's Republic of China*
[b] *State Key Laboratory of Organometallic Chemistry, Shanghai Institute of Organic Chemistry, Chinese Academy of Sciences, Shanghai 200032, People's Republic of China*
[c] *School of Materials Engineering, Changshu Institute of Technology, Changshu 215500, Jiangsu, People's Republic of China*
[d] *Department of Energy Science and Engineering, Nanjing Tech University, Nanjing 210000, Jiangsu, People's Republic of China*
[e] *Université de Strasbourg - CNRS, Institut de Chimie (UMR 7177 CNRS), 4 rue Blaise Pascal-CS 90032, 67081 Strasbourg, France*

ARTICLE INFO

ABSTRACT

Constructing heterojunction nanocomposites with optimized active sites and interface electronic structures is promising for hydrogen evolution reaction (HER). Herein, we present an interface engineering strategy to fabricate two heterostructures, triphase MoSe₂/NiSe-1 including 1T-MoSe₂, 2H-MoSe₂ and hexagonal phase NiSe (H-NiSe), and tetraphase MoSe₂/NiSe-2 including 1T-MoSe₂, 2H-MoSe₂, H-NiSe and rhombohedral phase NiSe (R-NiSe). MoSe₂/NiSe-1 exhibited remarkably enhanced HER activity with an overpotential of 30 mV at 10 mA cm^{-2}, and negligible voltage change even when operated for 40 h. The strong electronic synergistic interaction between the different interfaces of mixed MoSe₂/NiSe greatly enhanced the HER performance. Density functional theory calculations helped rationalize why the combination of three phases is more active, by increasing the interface electron concentration, facilitating electron transfer and decreasing the free energy ΔG_{H2O} and ΔG_{H*}. This work provides a rational strategy to design and assemble stable and high-performance multiphasic heterojunctioned HER electrocatalysts.

1. Introduction

The continuing search for more active and efficient non-noble metal electrocatalysts for hydrogen evolution reaction (HER) is of far-reaching significance for environmental and energy issues [1,2]. Transition-metal chalcogenides (TMCs) have been explored as one of key alternatives to noble metal catalysts toward HER owing to their intrinsic advantages of remarkable activity, low cost, earth abundance and environmental friendliness [3,4]. MoSe₂, as one of typical HER-active TMCs, has attracted much attention due to its adjustable active sites and superior stability [5,6]. The HER performance of MoSe₂ is greatly affected by its crystal phases (1T and 2H) and electronic structures [5,7,8]. The metallic-phase 1T-MoSe₂ possesses an excellent electronic conductivity, a larger interlayer spacing, and more electrochemically active sites in the basal plane, which is beneficial for HER [9]. Furthermore, the nonlayered metal chalcogenide NiSe with several phases, including

hexagonal, orthorhombic and rhombohedral, also has emerged as a promising catalyst for water electrolysis, especially in alkaline HER [10–14]. However, the electronic transport capacity of a single phase electrocatalyst is generally poor and its HER performance is easy to reach a plateau [15,16]. As Mo and Ni lie on the left-hand side of the volcano plot and possess excessively high H* adsorption strengths, single phase MoSe₂ or NiSe shows much lower HER activity than Pt [17].

As a new type of catalysts, heterojunction nanocomposites provide new feasibilities for enhancing HER activity and have received widespread attention [18–20]. Heterojunctions composed of two or more phases can compensate for the shortcomings of each single phase and optimize the inherent active species, active sites and electrical conductivity to generate synergistic interactions between them, thereby promoting HER catalytic performance [21,22]. Interface engineering is deemed as an elegant approach in achieving heterojunction nanocomposites [23–26]. Thus if HER-active NiSe and MoSe₂ phases could be

---

combined via interface engineering, the resulting MoSe$_2$/NiSe heterojunction catalysts may display greatly improved HER catalytic performances. For example, Hu et al. reported the successful preparation of 1 T-MoSe$_2$/NiSe heterostructure nanowire arrays for synergistically enhanced HER with high intrinsic activity for water dissociation and H$_2$ formation [27]. The electronic injection from NiSe into MoSe$_2$ induced the phase transition from 2 H-MoSe$_2$ to 1T-MoSe$_2$. This heterostructure presented good electrocatalytic activity for the HER with a low overpotential of 200 mV at 50 mA cm^{-2}. However, the precise control of the heterostructure combined with three or more phases is rarely explored, which is unfavorable for us to in-depth understand the relationship between interface electronic structure and electrocatalytic HER activity. Therefore, developing high-performance heterostructure electrocatalysts toward HER remains a great challenge [21,28,29].

Herein, we proposed an interface engineering method based on the hydrothermal selenylation of NiMoO$_4$ nanorods to construct two uncommon MoSe$_2$/NiSe heterojunction nanocomposites including a triphase nanohybrid (denoted as MoSe$_2$/NiSe-1) composed of tetragonal phase MoSe$_2$ (1T-MoSe$_2$), hexagonal phase MoSe$_2$ (2H-MoSe$_2$) and hexagonal phase NiSe (H-NiSe) and a tetraphase nanohybrid (denoted as MoSe$_2$/NiSe-2) made up of 1T-MoSe$_2$, 2H-MoSe$_2$, H-NiSe and rhombohedral phase NiSe (R-NiSe). The precursor NiMoO$_4$ nanorods provided the feasibility to construct multiphasic heterojunctions between HER-active NiSe and MoSe$_2$ phases. Compared to single phase NiSe or MoSe$_2$, triphase MoSe$_2$/NiSe-1 exhibited remarkably enhanced HER activity with an overpotential of 30 mV at 10 mA cm^{-2} and a negligible voltage change, even when operated at a current density of 10 mA cm^{-2} for 40 h. Such a great enhancement results from the triumphant modulation of interfacial electronic structure of this heterojunction. Density functional theory (DFT) calculations revealed that the combination of 1T/2H-MoSe$_2$ and H-NiSe results in a high electrical conductivity and a decrease of the water dissociation and H$_2$ formation energy in the HER. The electronic distribution at the interfaces of MoSe$_2$/NiSe-1 is more uniform than MoSe$_2$/NiSe-2, which facilitates electron transport and promotes HER activity. This work provides useful insights into complex multiphasic systems and opens up a promising way to construct multiphasic heterojunction electrocatalysts for HER.

2. Experimental section

2.1. Preparation of NiMoO$_4$ nanorods on NF

The reaction solution was obtained by mixing 0.5 mmol of Ni (NO$_3$)$_2$·6H$_2$O and 0.5 mmol of Na$_2$MoO$_4$·2H$_2$O in 15 ml distilled water under constant magnetic stirring and then transferred into a Teflon-lined stainless-steel autoclave and NF (2 × 2.5 cm) was added. The autoclave was sealed and maintained at 150 °C for 6 h. The products were taken out and cleaned by ultrasonication for several minutes to remove the loosely attached materials on their surface before drying at 60 °C overnight under vacuum. In order to obtain crystallized NiMoO$_4$ nanostructures, the conductive substrates with as-grown precursor hierarchical structures were calcined at 450 °C for 2 h in argon atmosphere.

2.2. Preparation of MoSe$_2$/NiSe-1

First, 2/3 mmol Se powder was dissolved in 1.6 ml N$_2$H$_4$·H$_2$O and then 8.4 ml distilled H$_2$O containing 1/3 mmol Na$_2$MoO$_4$·2H$_2$O was added. The obtained solution was transferred into Teflon-lined stainless-steel autoclave and NiMoO$_4$-NF (2 × 2.5 cm) was added. The autoclave was sealed and maintained at 200 °C for 3 h. After cooling down to room temperature, the products were taken out and rinsed thoroughly with DI water, ethanol and dried at 60 °C overnight.

2.3. Preparation of MoSe$_2$/NiSe-2

First, 2/3 mmol Se powder was dissolved in 1.6 ml N$_2$H$_4$·H$_2$O and then 8.4 ml distilled H$_2$O was added. The solution was transferred into a Teflon-lined stainless-steel autoclave and NiMoO$_4$-NF (2 × 2.5 cm) was added. The autoclave was sealed and maintained at 200 °C for 3 h. After cooling down to room temperature, the products were taken out and rinsed thoroughly with DI water, ethanol and dried at 60 °C overnight.

2.4. Characterization

Powder X-ray diffraction (PXRD) was carried out on an X′Pert-Pro MPD diffractometer (Netherlands PANalytical) using a Cu Kα X-ray source (λ = 1.540598 Å) operated at 40 kV and 15 mA. Raman spectra were collected on LabRam Armis IR2 (Horiba) and the laser wavelength is 633 nm. Scanning electron microscopy (SEM) images were obtained with a HITACHI S-4700 cold field-emission scanning electron microscope operated at 15 kV. Transmission electron microscopy (TEM) images were obtained with a HITACHI HT7700 operated at 80 kV. High-resolution TEM (HRTEM), high angle annular dark field scanning TEM (HAADF-STEM), selected-area electron diffraction (SAED) and elemental mapping were performed on a FEI Tecnai F20 transmission electron microscope at an acceleration voltage of 200 kV. The X-ray photoelectron spectra (XPS) were recorded on an SSI S-Probe XPS spectrometer.

2.5. Electrochemical measurements

Electrochemical measurements were performed on a CHI 660E electrochemical analyzer (Chenhua, Shanghai) with a conventional three electrode arrangement consisting of NF (0.5 cm × 1 cm) as working electrode, platinum foil as the counter electrode, and Ag/AgCl as the reference electrode. Polarization curves were obtained using linear sweep voltammetry (LSV) with a scan rate of 5 mV s^{-1} in 1 M KOH. The HER was conducted without any iR drop compensation. The long-term durability test was performed using chronopotentiometric measurements, which were also carried out without compensating for iR drop. The electrochemical surface area (ECSA) was estimated from the electrochemical double-layer capacitance (C$_{dl}$) using cyclic voltammetry (CV) in a non-faradaic potential range at various scan rates including 20, 40, 60, 80 and 100 mV s^{-1}. The reference electrode was calibrated to the reversible hydrogen electrode (RHE): E (RHE) = E (Ag/AgCl) + (0.197 + 0.059 pH).

2.6. Computational methods

We have employed the first-principles to perform all the density functional theory (DFT) calculations within the generalized gradient approximation (GGA) using the PBE formulation [30–32]. We have chosen the projected augmented wave (PAW) potentials to describe the ionic cores and taken valence electrons into account using a plane wave basis set with a kinetic energy cutoff of 450 eV [33,34]. Partial occupancies of the Kohn−Sham orbitals were allowed using the Gaussian smearing method and a width of 0.05 eV. The electronic energy was considered self-consistent when the energy change was smaller than 10^{-4} eV. A geometry optimization was considered convergent when the force change was smaller than 0.05 eV/Å. Grimme's DFT-D3 methodology was used to describe the dispersion interactions [35]. During structural optimizations, the 2 × 2 × 1 Monkhorst-Pack k-point grid for Brillouin zone was used for k-point sampling for structures. Finally, the adsorption energies (E$_{ads}$) were calculated as E$_{ads}$ = E$_{ad/sub}$ - E$_{ad}$ - E$_{sub}$, where E$_{ad/sub}$, E$_{ad}$, and E$_{sub}$ are the total energies of the optimized adsorbate/substrate system, the adsorbate in the structure, and the clean substrate, respectively. The free energy was calculated using the equation:

$$G = E + ZPE - TS$$

where G, E, ZPE and TS are the free energy, total energy from DFT

calculations, zero point energy and entropic contributions, respectively. In our calculation, the U correction had been set as 3.96 eV for Ni atoms in our systems. In addition, the density of states had been calculated using the $3 \times 3 \times 2$ Monkhorst-Pack k-point sampling.

3. Results and discussion

3.1. Structure, morphology, and composition analyses

The formation procedures of MoSe₂/NiSe-1 and MoSe₂/NiSe-2 by selenylation of NiMoO₄-NF (NF = nickel foam) are schematically illustrated in Scheme 1 and Scheme S1, respectively. First, NiMoO₄ nanorods on NF were obtained by hydrothermal reaction between Na₂MoO₄ and Ni(NO₃)₂ (molar ratio = 1: 1) in the presence of NF at 150 °C followed by calcination at 450 °C in an argon atmosphere. The as-prepared nanorods are distributed uniformly on the surface of NF (Figs. S1-S2). When NiMoO₄ nanorods on NF were hydrothermally treated with an aqueous solution containing Se powder and N₂H₄•H₂O in the presence of additional Na₂MoO₄ at 200 °C, a rare triphase nanohybrid MoSe₂/NiSe-1 on NF was yielded. Its nanosheets morphology was totally different from that of the original NiMoO₄ nanorods on NF (Fig. 1a and b). Intriguingly, direct selenylation of NiMoO₄ without additional Na₂MoO₄ results in another uncommon multiphase nanocomposite MoSe₂/NiSe-2, in which 1T-MoSe₂, 2H-MoSe₂, and H-NiSe are integrated with R-NiSe. In this case, the resulting tetraphase MoSe₂/NiSe-2 inherited a similar nanorod morphology to its parent NiMoO₄, but the original smooth nanorod surface was decorated with nanosheets (Fig. S3a and S3b). With these two selenylation-induced heterojunctions in hand, we employed selected area electron diffraction (SAED) and high resolution transmission electron microscopy (HRTEM) to reveal their phase compositions and structures. For MoSe₂/NiSe-1, the SAED pattern in Fig. 1c evidences the polycrystallinity of MoSe₂ and NiSe. The seven unambiguous diffraction rings belong to the crystal planes of (102), (105) and (213) of MoSe₂ (JCPDS No. 00–020–0757) and to the (102), (201), (004) and (211) planes of H-NiSe (JCPDS No. 00–002–0892). The HRTEM images further revealed the well-defined interfacial structure between MoSe₂ and NiSe. Since they were derived from the same precursor, the interfacial coupling of MoSe₂ and NiSe was seamless. As shown in Figs. 1d, S4 and S5, the orange dotted line is the interface between MoSe₂ and NiSe and we can observe distinctly different lattice fringes on both sides of interface. The interplanar spacing of 0.64 nm corresponds to the (002) plane of MoSe₂ [36,37], while the interplanar spacings of 0.27 nm and 0.20 nm are ascribed to the (101) and (102) planes of H-NiSe, respectively [13,38,39]. The lattice fringes in Fig. S6 belong to the H-NiSe phase. The trigonal lattice in the area marked by the green coil implies the presence of 1 T-MoSe₂, while the hexagonal lattice in the yellow coil suggests the presence of 2H-MoSe₂ (Figs. 1e and S7), thereby

indicating the successful fabrication of 1T/2H-MoSe₂ [5]. The EDS elemental mapping images reveal the rather uniform distribution of the Mo, Se and Ni elements in the nanosheets (Fig. 1f). As shown in Fig. S8, the molar ratio of Mo, Se and Ni (1:3.44:1.58) is consistent with the norminal composition. It is worth noting that the percentage of MoSe₂ and NiSe should be 1:1 theoretically in the heterostructure due to the molar ratio of Ni to Mo is 1:1 in the precursor NiMoO₄. However, we used NF as the substrate to support anchoring of other phases. NF was also involved in the reaction with selenide and the actual ratio of NiSe to MoSe₂ would be somewhat higher than 1: 1. Similarly, the SAED and HRTEM images of MoSe₂/NiSe-2 also indicate the multi-heterojunction interfaces of 1T-MoSe₂, 2H-MoSe₂, H-NiSe and R-NiSe (Fig. S3c-S3d). The interplanar spacings of 0.26 nm, 0.32 nm and 0.64 nm correspond to the (021) plane of R-NiSe, (100) plane of H-NiSe and (002) plane of 2H-MoSe₂, respectively [13]. Fig. S3e also demonstrates the presence of 2H phase and 1T phase of MoSe₂. Corresponding EDS spectrum and elemental mapping images obtained for MoSe₂/NiSe-2 confirmed the uniform distribution of Mo, Ni and Se elements (Figs. S3f and S9).

The conversion of NiMoO₄ to triphase MoSe₂/NiSe-1 through in situ selenylation can be further confirmed by the PXRD and Raman spectroscopy (Fig. 2a-b). The obvious diffraction peaks at 27.8°, 32.7°, 44.3°, 49.9°, 59.5°, 61.1°, 69.1°, 70.4° and 82.8° can be indexed to the (100), (101), (102), (110), (103), (201), (202), (004), (203) and (211) crystal planes of H-NiSe (JCPDS No. 00–002–0892). No obvious diffraction peaks of MoSe₂ can be observed in Fig. 2a due to its low crystallinity. Similarly, the broadened diffraction peaks observed for the bare MoSe₂ nanosheets reveal their relatively low crystallinity (Fig. S10) [40]. However, the Raman spectrum shows two signals at 240 and 285 cm⁻¹ (Fig. 2b), typical of 2H-MoSe₂, while the peaks at 195, 350, and 480 cm⁻¹ clearly confirmed the existence of 1T-MoSe₂ [27,41,42]. The PXRD patterns of MoSe₂/NiSe-2 are shown in Fig. S11a. The peaks at 17.8°, 31.0°, 34.1°, 38.7°, 46.5°, 50.4°, 55.1° and 56.0° are ascribed to the R-NiSe (110), (300), (021), (211), (131), (401), (330) and (012) crystal planes, respectively (JCPDS No. 00–18–0887), confirming the emergence of the fourth phase. The Raman spectrum also reveals the co-existence of 1T-MoSe₂ and 2H-MoSe₂ in MoSe₂/NiSe-2 (Fig S11b). Next, XPS spectra are used to examine the valence states and binding energies of the elements in MoSe₂/NiSe-1 and MoSe₂/NiSe-2. The high-resolution XPS spectra of Mo 3d, Se 3d, Ni 2p and O 1 s in MoSe₂/NiSe-1 are presented in Fig. 2c-f, respectively. The two main peaks at 231.6 and 228.8 eV, corresponding to Mo $3d_{3/2}$ and Mo $3d_{5/2}$, are ascribed to 1T-MoSe₂, whereas the peaks located at 232.8 and 229.4 eV belong to 2H-MoSe₂. The peak at 235.6 eV is assigned to Mo⁶⁺ $3d_{3/2}$ and arises from the partial air oxidation of Mo⁴⁺ [43]. According to the integrated area of the relative intensity peaks, the ratio of 1T phase to 2H phase could be approximately 1: 0.7. Likewise, the peaks of Se 3d can also be deconvoluted into two pairs of peaks, at 53.8 and
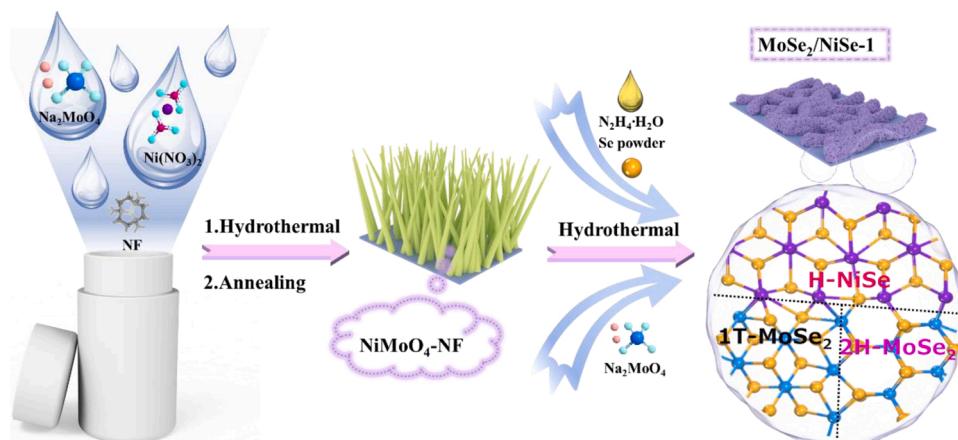
Scheme 1. Synthetic procedure for the triphase heterojunction HER electrocatalyst MoSe₂/NiSe-1.
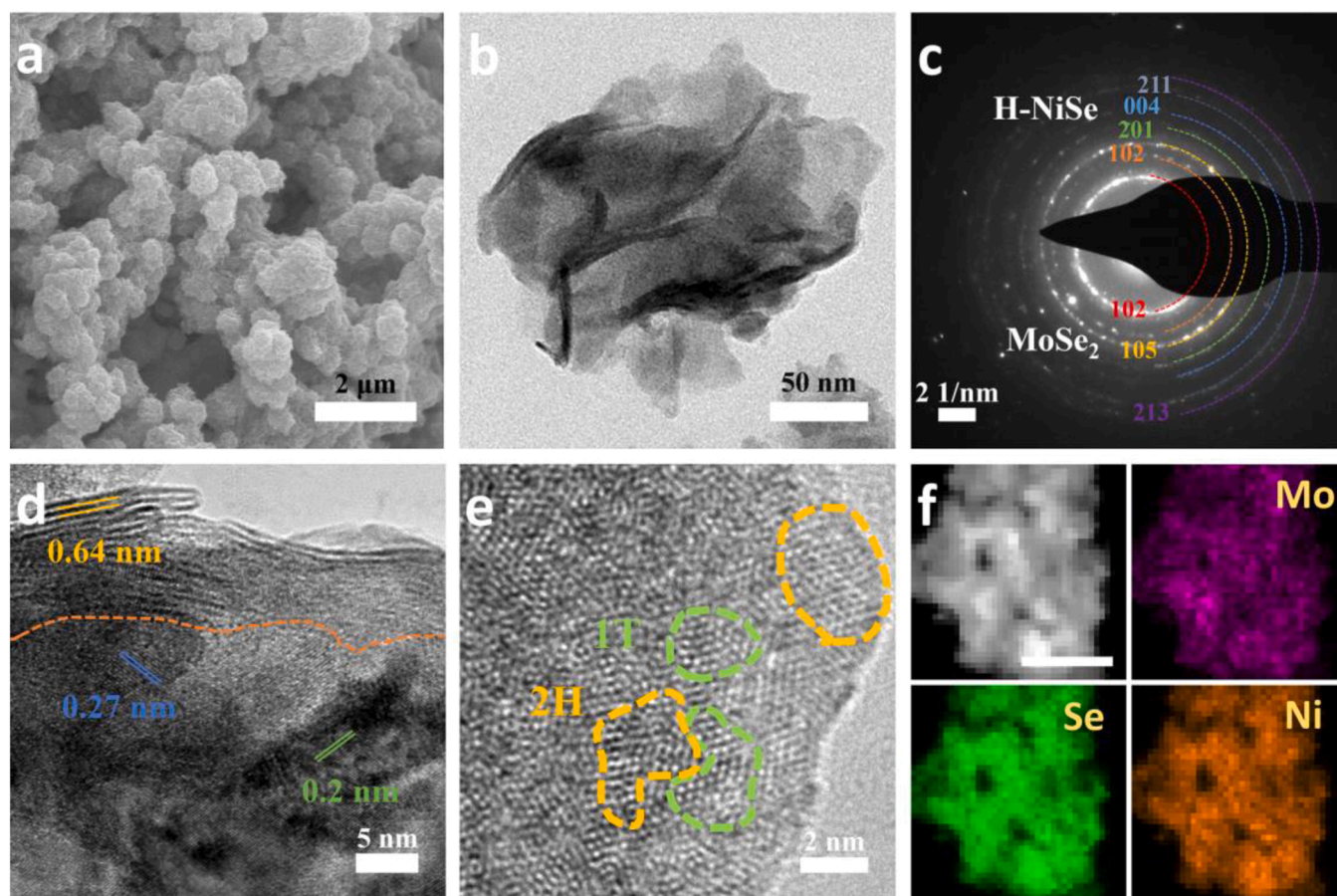
Fig. 1. (a) SEM, (b) TEM, (c) SAED, (d-e) HRTEM and (f) EDS elemental mapping images of $MoSe_2/NiSe-1$.
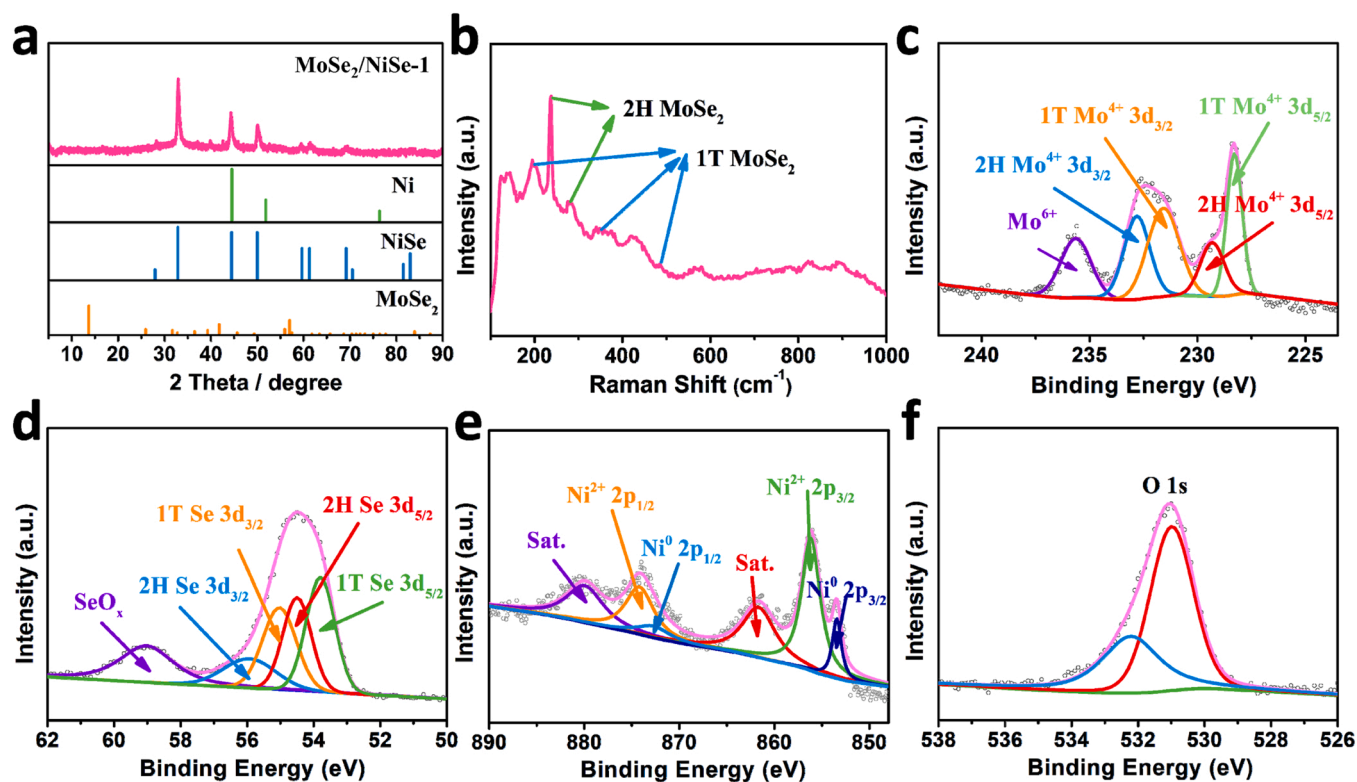

Fig. 2. (a) PXRD patterns, (b) Raman spectrum, high-resolution XPS spectra in the Mo 3d (c), Se 3d (d), Ni 2p (e) and O 1 s (f) regions of $MoSe_2/NiSe-1$.

55.0 eV and at 54.5 and 56.0 eV, suggesting the existence of 1T/2H-MoSe$_2$. The broad peak centered at 59.0 eV corresponds to SeO$_X$ species originating from partial oxidation of Se^{2-} on the surface [36,37]. The Ni 2p spectrum can be deconvoluted into six peaks, corresponding to Ni (853.4 and 872.7 eV), Ni^{2+} (856.2 and 874.3 eV) and satellites (861.7 and 880.1 eV). Compared to those of 1T/2H-MoSe$_2$ and H-NiSe, the binding energy of Mo 3d in MoSe$_2$/NiSe-1 is downshifted while that of Ni 2p is upshifted, which suggests some electron transfer and reconfiguration of the electronic structure between H-NiSe and 1T/2H-MoSe$_2$ (Fig. S12). The electron transfer to transition-metal dichalcogenides (TMDs) would result in the increase of Dd-orbital electron density of the transition metal [27]. Therefore the electron transfer from Ni center to Mo center through the interface led to the change in binding energy. In the high-resolution XPS spectrum of O 1 s, there are two distinct peaks at 531.0 and 532.2 eV, which correspond to some residual oxygen and

hydroxyl species on the surface (contributed by adsorbed water molecules), respectively [44,45]. A similar analysis was performed on MoSe$_2$/NiSe-2 and the ratio of 1T-MoSe$_2$ to 2H-MoSe$_2$ in it is close to 1: 1 (Fig. S11c-S11f). The difference of binding energies demonstrates the different electronic structures between MoSe$_2$/NiSe-2 and MoSe$_2$/NiSe-1 (Fig. S13).

3.2. Electrochemical HER performance

We then examined the electrochemical performances of MoSe$_2$/NiSe-1 and MoSe$_2$/NiSe-2 in 1 M KOH for H$_2$ production. For a better comparison, we also synthesized different NiSe and MoSe$_2$ single phases and their combinations as control samples and characterized them in detail (Figs. S14-S28). Although 1T-MoSe$_2$ is known to show better performance than 2H-MoSe$_2$, 1T-MoSe$_2$ is unstable and easy to be
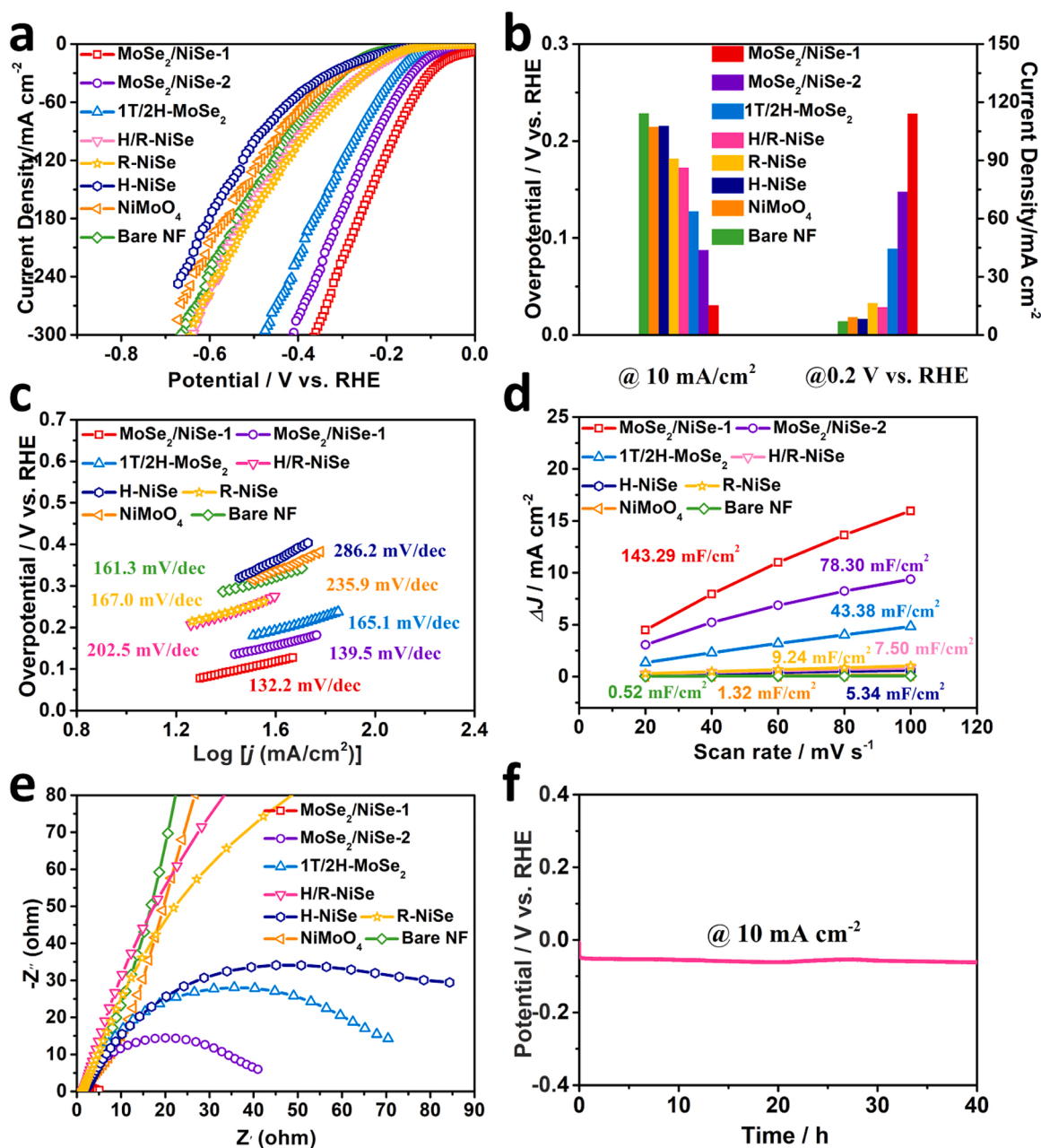
Fig. 3. (a) LSV curves, (b) The corresponding overpotentials and current densities of different catalysts at 10 mA cm^{-2} and − 0.2 V vs. RHE, (c) Tafel plots, (d) C$_{dl}$, (e) Nyquist plots of bare NF, NiMoO$_4$-NF, H-NiSe-NF, R-NiSe-NF, H/R-NiSe-NF, 1T/2H-MoSe$_2$-NF, MoSe$_2$/NiSe-1 and MoSe$_2$/NiSe-2. (f) Chronopotentiometric curve of MoSe$_2$/NiSe-1.

converted into 2H phase [7]. Thus we always obtained the mixed phase of 1T-MoSe$_2$ and 2H-MoSe in this complex system. The MoSe$_2$/NiSe-1 and MoSe$_2$/NiSe-2 displayed significantly reduced overpotentials of 30 mV and 87 mV at 10 mA cm^{-2} in comparison to 1T/2H-MoSe$_2$ (127 mV), H/R-NiSe (172 mV), H-NiSe (215 mV), R-NiSe (182 mV), NiMoO$_4$ (214 mV) and bare NF (228 mV), as shown in linear sweep voltammetry (LSV) curves (Fig. 3a). These results demonstrated that only combining MoSe$_2$ and NiSe together can enhance the HER performance dramatically. The HER performance of MoSe$_2$/NiSe-1 is superior to commercial Pt/C (20%), while the catalytic performance of MoSe$_2$/NiSe-2 is weaker than that of Pt/C (20%) (Fig. S29). The MoSe$_2$/NiSe-1 electrode displayed the largest current density of 114 mA cm^{-2} at − 0.2 V (Fig. 3b). To gain an in-depth understanding of the HER kinetic mechanism, we calculated the Tafel slopes of these electrodes without any *iR* drop compensation and obtained small slopes of 132.2 and 139.5 mV/dec for the MoSe$_2$/NiSe-1 and MoSe$_2$/NiSe-2 electrodes, respectively (Fig. 3c). The electrochemical active specific area (ECSA) was calculated by measuring the double-layer capacitance (C$_{dl}$) based on the CV results at different scan rates in the non-Faraday region (Fig. S30). The measured current density is plotted as a function of scan rate in Fig. 3d. Noticeably, the MoSe$_2$/NiSe-1 electrode possessed the highest C$_{dl}$ value of 143.29 mF cm^{-2}, substantially larger

than those of MoSe$_2$/NiSe-2 (78.30 mF cm^{-2}), 1T/2H-MoSe$_2$ (43.38 mF cm^{-2}), H/R-NiSe (7.50 mF cm^{-2}), H-NiSe (5.34 mF cm^{-2}), R-NiSe (9.24 mF cm^{-2}), NiMoO$_4$ (1.32 mF cm^{-2}) and bare NF (0.52 mF cm^{-2}), suggesting that the multi-heterogeneous interfaces of MoSe$_2$/NiSe-1 have more active sites exposed.

In addition, electrochemical impedance spectroscopy (EIS) measurements were carried out to investigate the electrochemical reaction kinetics during the HER process. The semicircle shown in the Nyquist plot (Fig. 3e) indicates the charge transfer resistance (R$_{ct}$) of the H$^+$ reaction between the electrode and electrolyte [46]. Specifically, the MoSe$_2$/NiSe-1 electrode presents the lowest value for R$_{ct}$, suggesting the fastest charge transfer kinetics and conductivity. Furthermore, the MoSe$_2$/NiSe-1 electrode shows excellent long-term durability with a negligible voltage change, even when operated for 40 h at a current density of 10 mA cm^{-2}, as shown in Fig. 3f. We also examined its stability at a large current density of 200 mA cm^{-2}, which showed no significant decrease in catalytic performance after 20 h (Fig. S31). To check the stability of MoSe$_2$/NiSe-1, EDS, PXRD, Raman and XPS experiments were performed after HER cycling. As shown in Figs. S32-S33, the elemental compositions were consistent with the original ones and the mixed 1T/2H-MoSe$_2$ and H-NiSe phases still coexisted. Moreover, the Se 3d, Mo 3d and Ni 2p spectra after HER
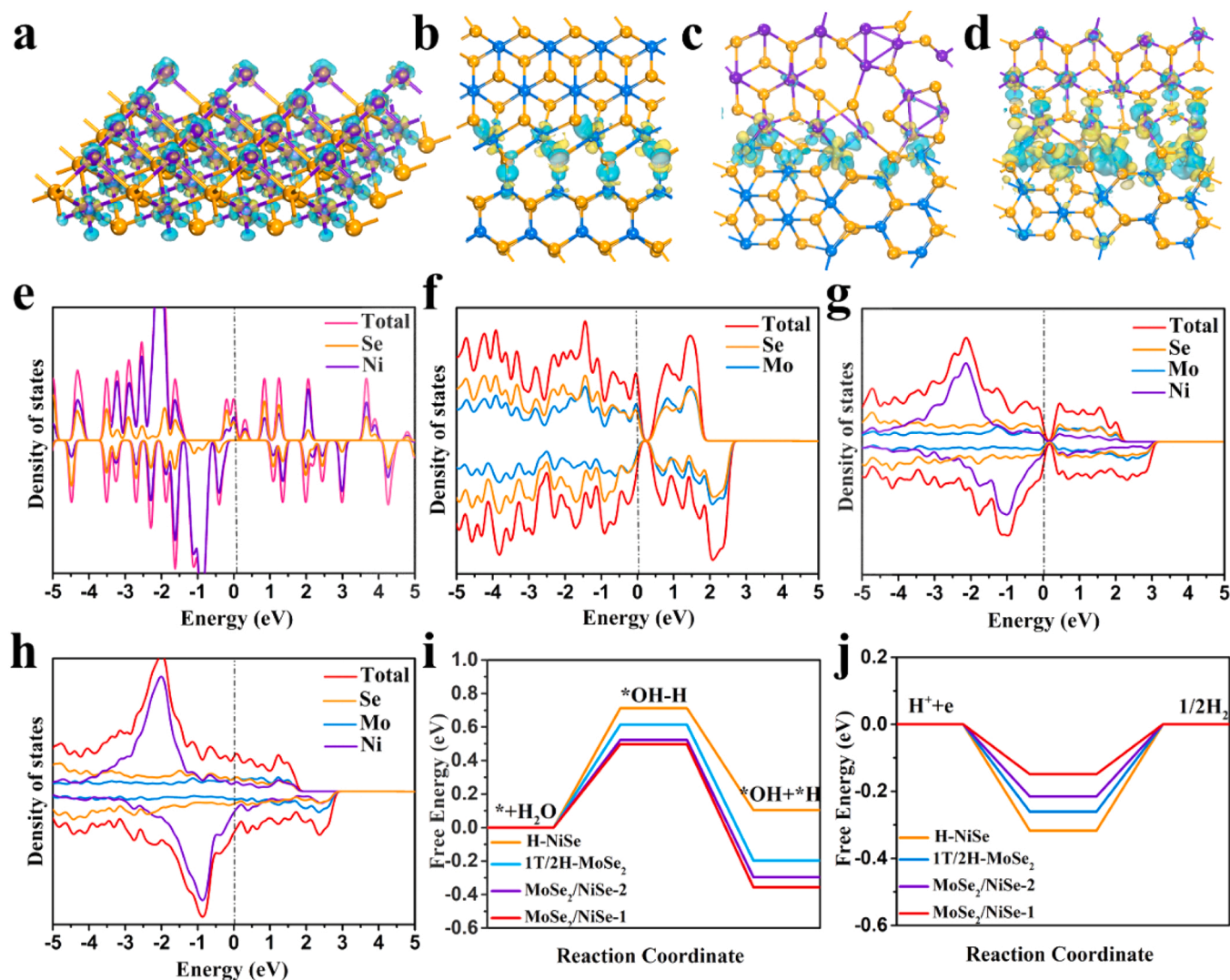
Fig. 4. Spatial map of charge density differences for (a) H-NiSe, (b) 1T/2H-MoSe$_2$, (c) MoSe$_2$/NiSe-2 and (d) MoSe$_2$/NiSe-1. Regions of electron accumulation and depletion are denoted by blue and yellow lobes, respectively. Projected densities of states of (e) H-NiSe, (f) 1T/2H-MoSe$_2$, (g) MoSe$_2$/NiSe-2 and (h) MoSe$_2$/NiSe-1. Fermi level is denoted by dashed black lines. Free energy diagram of (i) water dissociation and (j) hydrogen evolution.

cycling did not show obvious changes compared to their initial ones. Thus, MoSe$_2$/NiSe-1 is demonstrated as an efficient catalyst with excellent HER activity in alkaline solution.

3.3. Theoretical calculations

DFT calculations were performed to gain further insight into the synergistic effect of MoSe$_2$/NiSe-1 and MoSe$_2$/NiSe-2 multi-heterogeneous interfaces in the HER. We adopted the models in Fig. S34 to showcase the evolution of the atomic adsorption on different substrates. The epitaxial relationship in the MoSe$_2$-NiSe system originates from the selenium layers. There are many active sites in the two heterojunction nanocomposites, but Ni atoms are assumed to be the most active centers according to DFT calculations. These sites efficiently enabled water adsorptive dissociation and hydrogen evolution. First, we investigated the interfacial electron interaction (Fig. 4a-d). Compared to bare H-NiSe and 1 T/2 H-MoSe$_2$, the interfacial electron concentrations of MoSe$_2$/NiSe-1 and MoSe$_2$/NiSe-2 are significantly increased, indicating much stronger electron orbital coupling in the heterostructures, which results in more conductive catalysts with faster charge transfer and dramatically improved activity [47,48]. In addition, compared to the triphase heterostructure, the emergence of an extra-phase R-NiSe in MoSe$_2$/NiSe-2 results in an uneven electron distribution at the interface, which leads to decreased electron transfer and electron density at the interface. These effects hinder the electron conduction and reduce the HER activity with inferior performances of MoSe$_2$/NiSe-2 compared to MoSe$_2$/NiSe-1. In this case, too many interfaces might cause uneven electron distribution and inhibit electron transport, and do not result in better catalytic performances. To better understand the surface electronic structure reconfiguration, the projected density of states (PDOS) of H-NiSe, 1T/2H-MoSe$_2$, MoSe$_2$/NiSe-1 and MoSe$_2$/NiSe-2 were obtained. As disclosed by the total density of states of MoSe$_2$/NiSe-1 and MoSe$_2$/NiSe-2, the electron densities near the Fermi level of the heterostructures are higher than those of H-NiSe and 1T/2H-MoSe$_2$ (Fig. 4e-f). This results from the strong interfacial interaction between NiSe and MoSe$_2$, indicating an enhanced electronic conductivity. According to the Dd-band center theory, the electron density around the Fermi level has a great impact on the binding energy of the reaction intermediate [49,50]. The number of electrons occupying the Fermi level of MoSe$_2$/NiSe-2 is less than that of MoSe$_2$/NiSe-1, there still exists a small band gap, while there is basically no band gap in MoSe$_2$/NiSe-1. Thus, the electron mobility of MoSe$_2$/NiSe-1 is more favorable, which is consistent with the EIS test results. According to the above analysis, the regulation of heterostructures could significantly influence the modulation of the interface electronic structure, optimize the conductivity and charge transfer kinetics and facilitate the HER process.

Generally, the reaction pathway of the HER process in alkaline media undergoes the following four steps: initial adsorption of H$_2$O on the catalyst, H$_2$O dissociation (Volmer), formation of the H* intermediate, and the H$_2$ generation (Tafel or Heyrovsky) [51,52]. The reaction pathways are listed as follows:

$$H_2O + M + e^- \rightarrow M\text{-}H + OH^- \text{ (Volmer)}$$

$$M\text{-}H + H_2O + e^- \rightarrow M + H_2 + OH^- \text{ (Heyrovsky)}$$

$$2M\text{-}H \rightarrow 2M + H_2 \text{ (Tafel)}$$
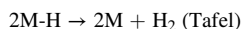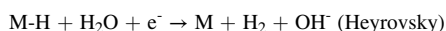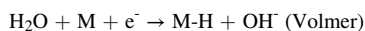
The free energy differences between the first and second steps, ΔG_{H2O}, and between the third and fourth steps, ΔG_{H*} are widely considered as critical indicators of the ability of hydrogen evolution [53,54]. The calculated Gibbs free energy diagrams are given in Fig. 4i and j. For H-NiSe and 1T/2H-MoSe$_2$, the water dissociation barriers of HER are as high as 0.71 and 0.61 eV, which are difficult to overcome. ΔG_{H2O} of MoSe$_2$/NiSe-2 and MoSe$_2$/NiSe-1 decrease to 0.52 and 0.49 eV, implying improved kinetics upon the Volmer step of HER. These results are in good agreement with the experimental observations.

High-efficiency HER catalysts should possess a ΔG_{H*} of near zero. As shown in Fig. 4j, the calculated ΔG_{H*} for H-NiSe and 1T/2H-MoSe$_2$ is approximately -0.32 and -0.26 eV, respectively, deviating greatly from the best value for the HER. The value of ΔG_{H*} for MoSe$_2$/NiSe-2 is -0.21 eV, which is much closer to the thermoneutral value than that of H-NiSe and 1T/2H-MoSe$_2$. For MoSe$_2$/NiSe-1, the ΔG_{H*} value is reduced to -0.14 eV, suggesting that the smallest reaction barrier between adsorption and desorption processes results in higher HER performances. These results reveal that the electrocatalytic activity can be effectively regulated and enhanced by the modulation of the catalyst electronic structure through construction of proper multiphase heterostructures.

4. Conclusion

In summary, we have successfully constructed two unusual multiphasic electrocatalysts, triphase MoSe$_2$/NiSe-1 and tetraphase MoSe$_2$/NiSe-2, by hydrothermal selenide implantation. The two heterojunction nanocomposites showed different electronic structures of the interfaces which are tuned by combining different MoSe$_2$ and NiSe phases. The two nanohybrids exhibited enhanced electrochemical performance for HER catalysis, only need overpotentials of 30 mV and 87 mV, respectively, to drive a current density of 10 mA cm^{-2}. The diverse multi-interfaces in MoSe$_2$/NiSe-1 and MoSe$_2$/NiSe-2 can be considered as versatile electroactive sites for fast electron transfer due to the occurrence of unique synergistic effects. DFT calculations revealed that compared to that of tetraphase MoSe$_2$/NiSe-2, the electronic distribution at the interfaces of triphase MoSe$_2$/NiSe-1 is more uniform, which results in a higher electron density, better conductivity and greater activity for HER. The protocol reported here is expected to inspire the design and preparation of more multiphasic heterojunction nanocomposites from different phases like MX$_2$, MX and MO (M = metal; X = chalcogenide) for efficient electrocatalytic energy-related reactions like HER, oxygen evolution reaction (OER), oxygen reduction reaction (ORR) and nitrogen reduction reaction (NRR).

CRediT authorship contribution statement

Jiang-Yan Xue: Conceptualization, Investigation, Writing – original draft, Funding acquisition. **Fei-Long Li:** Writing – review & editing, Funding acquisition. **Bingbing Chen:** Methodology, Software. **Hongbo Geng:** Writing – review & editing. **Wei Zhang:** Investigation. **Wan-Ying Xu:** Investigation. **Hongwei Gu:** Writing – review & editing. **Pierre Braunstein:** Writing– review & editing. **Jian-Ping Lang:** Conceptualization, Writing – review & editing, Supervision, Funding acquisition.

Declaration of Competing Interest

The authors declare that they have no known competing financial interests or personal relationships that could have appeared to influence the work reported in this paper.

Appendix A. Supporting information

Supplementary data associated with this article can be found in the online version at doi:10.1016/j.apcatb.2022.121434.

References

[1] Z.W. Seh, J. Kibsgaard, C.F. Dickens, I. Chorkendorff, J.K. Nørskov, T.F. Jaramillo, Combining theory and experiment in electrocatalysis: Insights into materials design, Science 355 (2017) 4998–5009, https://doi.org/10.1126/science.aad4998.

[2] G.Q. Zhao, Y.Z. Jiang, S.X. Dou, W.P. Sun, H.G. Pan, Interface engineering of heterostructured electrocatalysts towards efficient alkaline hydrogen electrocatalysis, Sci. Bull. 66 (2021) 85–96, https://doi.org/10.1016/j.scib.2020.09.014.

[3] R. Lv, J.A. Robinson, R.E. Schaak, D. Sun, Y. Sun, T.E. Mallouk, M. Terrones, Transition metal dichalcogenides and beyond: synthesis, properties, and applications of single- and few-layer nanosheets, Acc. Chem. Res. 48 (2014) 56, https://doi.org/10.1021/ar5002846.

[4] Z.P. Liu, L. Zhao, Y.H. Liu, Z.C. Gao, S.S. Yuan, X.T. Li, N. Li, S.D. Mao, Vertical nanosheet array of 1T phase MoS_2 for efficient and stable hydrogen evolution, Appl. Catal. B: Environ. 246 (2019) 296–302, https://doi.org/10.1016/j.apcatb.2019.01.062.

[5] S.J. Deng, F. Yang, Q.H. Zhang, Y. Zhong, Y.X. Zeng, S.W. Lin, X.L. Wang, X.H. Lu, C.Z. Wang, L. Gu, X.H. Xia, J.P. Tu, Phase modulation of (1T–2H)-$MoSe_2$/TiC-C shell/core arrays via nitrogen doping for highly efficient hydrogen evolution reaction, Adv. Mater. 30 (2018), 1802223, https://doi.org/10.1002/adma.201802223.

[6] S.J. Deng, Y. Zhong, Y.X. Zeng, Y.D. Wang, Z.J. Yao, F. Yang, S.W. Lin, X.L. Wang, X.H. Lu, X.H. Xia, J.P. Tu, Directional construction of vertical nitrogen-doped 1T–2H $MoSe_2$/graphene shell/core nanoflake arrays for efficient hydrogen evolution reaction, Adv. Mater. 29 (2017), 1700748, https://doi.org/10.1002/adma.201700748.

[7] S.J. Deng, C.Z. Ai, M. Luo, B. Liu, Y. Zhang, Y.H. Li, S.W. Lin, G.X. Pan, Q.Q. Xiong, Q. Liu, X.L. Wang, X.H. Xia, J.P. Tu, Coupled biphase (1T–2H)-$MoSe_2$ on mold spore carbon for advanced hydrogen evolution reaction, Small 15 (2019), 1901796, https://doi.org/10.1002/smll.201901796.

[8] Z.D. Lei, J. Zhan, L. Tang, Y. Zhang, Y. Wang, Recent development of metallic (1T) phase of molybdenum disulfide for energy conversion and storage, Adv. Energy Mater. 8 (2018), 1703482, https://doi.org/10.1002/aenm.201703482.

[9] R. Kappera, D. Voiry, S.E. Yalcin, B. Branch, G. Gupta, A.D. Mohite, M. Chhowalla, Phase-engineered low-resistance contacts for ultrathin MoS_2 transistors, Nat. Mater. 13 (2014) 1128, https://doi.org/10.1038/nmat4080.

[10] S. Anantharaj, S.R. Ede, K. Sakthikumar, K. Karthick, S. Mishra, S. Kundu, Recent trends and perspectives in electrochemical water splitting with an emphasis on sulfide, selenide, and phosphide catalysts of Fe, Co, and Ni: a review, ACS Catal. 6 (2016) 8069–8097, https://doi.org/10.1021/acscatal.6b02479.

[11] S. Anantharaj, S. Noda, Nickel selenides as pre-catalysts for electrochemical oxygen evolution reaction: a review, Int. J. Hydrog. Energy 45 (2020) 15763–15784, https://doi.org/10.1016/j.ijhydene.2020.04.073.

[12] H. Wu, G., F. Zheng, G.W. Ho, Topotactic engineering of ultrathin 2D nonlayered nickel selenides for full water electrolysis, Adv. Energy Mater. 8 (2018) 1702704, https://doi.org/10.1002/aenm.201702704.

[13] L.L. Zhai, T.W.B. Lo, Z.L. Xu, J. Potter, J.Y. Mo, X.Y. Guo, C.C. Tang, S.C.E. Tsang, S.P. Lau, In situ phase transformation on nickel-based selenides for enhanced hydrogen evolution reaction in alkaline medium, ACS Energy Lett. 5 (2020) 2483–2491, https://doi.org/10.1021/acsenergylett.0c01385.

[14] D.F. Yu, Z. Li, G.Y. Zhao, H. Zhang, H. Aslan, J.W. Li, F.F. Sun, L. Zhu, B.S. Du, B. Yang, W.W. Cao, Y. Sun, F. Besenbacher, M. Yu, Porous ultrathin NiSe nanosheet networks on nickel foam for high-performance hybrid supercapacitors, ChemSusChem 13 (2020) 260–266, https://doi.org/10.1002/cssc.201901766.

[15] R. Subbaraman, D. Tripkovic, D. Strmcnik, K.-C. Chang, M. Uchimura, A. P. Paulikas, V. Stamenkovic, N.M. Markovic, Enhancing hydrogen evolution activity in water splitting by tailoring Li^+-Ni(OH)$_2$-Pt interfaces, Science 344 (2011) 1256, https://doi.org/10.1126/science.1211934.

[16] S. Wang, D. Zhang, B. Li, C. Zhang, Z.G. Du, H.M. Yin, X.F. Bi, S.B. Yang, Ultrastable in-plane 1T–2H MoS_2 heterostructures for enhanced hydrogen evolution reaction, Adv. Energy Mater. 8 (2018), 1801345, https://doi.org/10.1002/aenm.201801345.

[17] H.X. Wang, W.W. Fu, X.H. Yang, Z.Y. Huang, J. Li, H.J. Zhang, Y. Wang, Recent advancements in heterostructured interface engineering for hydrogen evolution reaction electrocatalysis, J. Mater. Chem. A 8 (2020) 6926–6956, https://doi.org/10.1039/C9TA11646J.

[18] A.K. Geim, I.V. Grigorieva, Van der Waals heterostructures, Nature 499 (2013) 419–425.

[19] H. Zheng, Y. Li, H. Liu, X. Yin, Y. Li, Construction of heterostructure materials toward functionality, Chem. Soc. Rev. 40 (2011) 4506–4524, https://doi.org/10.1039/C0CS00222D.

[20] S.V.P. Vattikuti, Heterostructure Nanomaterials: Latest Trends in Formation of Inorganic Heterostructures, in: S.M. Bhagyaraj, O.S. Oluwafemi, N. Kalarikkal, S. Thomas (Eds.), Synthesis of Inorganic Nanomaterials, Elsevier, Amsterdam, 2018, pp. 89–120.

[21] X.R. Zheng, X.P. Han, Y.H. Cao, Y. Zhang, D. Nordlund, J.H. Wang, S.L. Chou, H. Liu, C. Zhong, Y.D. Deng, W.B. Hu, Identifying dense $NiSe_2$/$CoSe_2$ heterointerfaces coupled with surface high-valence bimetallic sites for synergistically enhanced oxygen electrocatalysis, Adv. Mater. 32 (2020), 2000607, https://doi.org/10.1002/adma.202000607.

[22] X.Y. Zhang, J. Li, Y. Yang, S. Zhang, H.S. Zhu, X.Q. Zhu, H.H. Xing, Y.L. Zhang, B. L. Huang, S.J. Guo, E. Wang, Co_3O_4/$Fe_{0.33}Co_{0.66}$P interface nanowire for enhancing water oxidation catalysis at high current density, Adv. Mater. 30 (2018), 1803551, https://doi.org/10.1002/adma.201803551.

[23] Y.K. Liu, S. Jiang, L. Zhou, Z.H. Li, J.M. Li, M.F. Shao, Interface engineering of (Ni, Fe)S$_2$@MoS_2 heterostructures for synergetic electrochemical water splitting, Appl. Catal. B: Environ. 247 (2019) 107–114, https://doi.org/10.1016/j.apcatb.2019.01.094.

[24] J. Zhang, T. Wang, D. Pohl, B. Rellinghaus, R.H. Dong, S.H. Liu, X.D. Zhuang, X. L. Feng, Interface engineering of MoS_2/Ni_3S_2 heterostructures for highly enhanced electrochemical overall-water-splitting activity, Angew. Chem. Int. Ed. 55 (2016) 6702–6707, https://doi.org/10.1002/anie.201602237.

[25] C. Chen, H. Su, L.N. Lu, Y.S. Hong, Y.Z. Chen, K. Xiao, T. Ouyang, Y.L. Qin, Z. Q. Liu, Interfacing spinel $NiCo_2O_4$ and NiCo alloy derived N-doped carbon nanotubes for enhanced oxygen electrocatalysis, Chem. Eng. J. 408 (2021), 127814, https://doi.org/10.1016/j.cej.2020.127814.

[26] C.C. Liu, T. Gong, J. Zhang, X.R. Zheng, J. Mao, H. Liu, Y. Li, Q.Y. Hao, Z. L. L, Li P. Y, X.P. Meng, Z. Lin, R.H. Wang, Engineering Ni_2P-$NiSe_2$ heterostructure interface for highly efficient alkaline hydrogen evolution, Appl. Catal. B: Environ. 262 (2020), 118245, https://doi.org/10.1016/j.apcatb.2019.118245.

[27] X. Zhang, Y.Y. Zhang, W.J. Jiang, Q.H. Zhang, Y.G. Yang, L. Gu, J.S. Hu, L.J. Wan, Phase-controlled synthesis of 1T-$MoSe_2$/NiSe heterostructure nanowire arrays via electronic injection for synergistically enhanced hydrogen evolution, Small Methods 3 (2019), 1800317, https://doi.org/10.1002/smtd.201800317.

[28] W.B. Li, Q.Q. Song, M. Li, Y.F. Yuan, J.H. Zhang, N. Wang, Z.H. Yang, J.F. Huang, J. Lu, X.F. Li, Chemical heterointerface engineering on hybrid electrode materials for electrochemical energy storage, Small Methods 5 (2021), 2100444, https://doi.org/10.1002/smtd.202100444.

[29] Y. Li, J.W. Zhang, Q.G. Chen, X.H. Xia, M.H. Chen, Emerging of heterostructure materials in energy storage: a review, Adv. Mater. 33 (2021), 2100855, https://doi.org/10.1002/adma.202100855.

[30] G. Kresse, J. Furthmüller, Efficiency of ab-initio total energy calculations for metals and semiconductors using a plane-wave basis set, Comput. Mater. Sci. 6 (1996) 15–50, https://doi.org/10.1016/0927-0256(96)00008-0.

[31] G. Kresse, J. Furthmüller, Efficient iterative schemes for ab initio total-energy calculations using a plane-wave basis set, Phys. Rev. B 54 (1996) 11169–11186, https://doi.org/10.1103/PhysRevB.54.11169.

[32] J.P. Perdew, K. Burke, M. Ernzerhof, Generalized gradient approximation made simple, Phys. Rev. Lett. 77 (1996) 3865–3868, https://doi.org/10.1103/PhysRevLett.77.3865.

[33] G. Kresse, D. Joubert, From ultrasoft pseudopotentials to the projector augmented-wave method, Phys. Rev. B 59 (1999) 1758–1775, https://doi.org/10.1103/PhysRevB.59.1758.

[34] P.E. Blöchl, Projector augmented-wave method, Phys. Rev. B 50 (1994) 17953–17979, https://doi.org/10.1103/PhysRevB.50.17953.

[35] S. Grimme, J. Antony, S. Ehrlich, H.J. Krieg, A consistent and accurate ab initio parametrization of density functional dispersion correction (DFT-D) for the 94 elements H-Pu, J. Chem. Phys. 132 (2010), 154104, https://doi.org/10.1063/1.3382344.

[36] D. Vikraman, S. Hussain, S.A. Patil, L. Truong, A.A. Arbab, S.H. Jeong, S.H. Chun, J. Jung, H.S. Kim, Engineering $MoSe_2$/WS_2 hybrids to replace the scarce platinum electrode for hydrogen evolution reactions and dye-sensitized solar cells, ACS Appl. Mater. Interfaces 13 (2021) 5061–5072, https://doi.org/10.1021/acsami.0c19890.

[37] Z.Y. Zhang, S. Ye, J. Ji, Z.L. Li, F. Wang, Core/shell-structured $NiMoO_4$@$MoSe_2$/NixSey nanorod on Ni foam as a bifunctional electrocatalyst for efficient overall water splitting, Colloids Surf. A 599 (2020), 124888, https://doi.org/10.1016/j.colsurfa.2020.124888.

[38] V. Murugadoss, J. Lin, H. Liu, X. Mai, T. Ding, Z. Guo, S. Angaiah, Optimizing graphene content in a NiSe/graphene nanohybrid counter electrode to enhance the photovoltaic performance of dye-sensitized solar cells, Nanoscale 11 (2019) 17579–17589, https://doi.org/10.1039/C9NR07060E.

[39] Z.X. Zou, X.Y. Wang, J.S. Huang, Z.C. Wu, F. Gao, An Fe-doped nickel selenide nanorod/nanosheet hierarchical array for efficient overall water splitting, J. Mater. Chem. A 7 (2019) 2233–2241, https://doi.org/10.1039/C8TA11072G.

[40] M.R. Gao, J.X. Liang, Y.R. Zheng, Y.F. Xu, J. Jiang, Q. Gao, J. Li, S.H. Yu, An efficient molybdenum disulfide/cobalt diselenide hybrid catalyst for electrochemical hydrogen generation, Nat. Commun. 6 (2015) 5982, https://doi.org/10.1038/ncomms6982.

[41] D. Kong, H. Wang, J.J. Cha, M. Pasta, K.J. Koski, J. Yao, Y. Cui, Synthesis of MoS_2 and $MoSe_2$ films with vertically aligned layers, Nano Lett. 13 (2013) 1341, https://doi.org/10.1021/nl400258t.

[42] Y. Yin, Y.M. Zhang, T.L. Gao, T. Yao, X.H. Zhang, J.C. Han, X.J. Wang, Z.H. Zhang, P. Xu, P. Zhang, X.Z. Cao, B. Song, S. Jin, Synergistic phase and disorder engineering in 1T-MoSe2 nanosheets for enhanced hydrogen evolution reaction, Adv. Mater. 29 (2017), 1700311, https://doi.org/10.1002/adma.201700311.

[43] H.R. Inta, S. Ghosh, A. Mondal, G. Tudu, H.V.S.R.M. Koppisetti, V. Mahalingam, $Ni_{0.85}$Se/$MoSe_2$ interfacial structure: an efficient electrocatalyst for alkaline hydrogen evolution reaction, ACS Appl. Energy Mater. 4 (2021) 2828–2837, https://doi.org/10.1021/acsaem.1c00125.

[44] C.C. Wang, D.T. Wu, Y. Qin, Y. Kong, Nanowired $NiMoO_4$/$NiSe_2$/$MoSe_2$ prepared through in situ selenylation as a high performance supercapacitor electrode, Chem. Commun. 57 (2021) 4019–4022, https://doi.org/10.1039/D1CC00461A.

[45] C. Qing, C.X. Yang, M.Y. Chen, W.H. Li, S.Y. Wang, Y.W. Tang, Design of oxygen-deficient NiMoO$_4$ nanoflake and nanorod arrays with enhanced supercapacitive performance, Chem. Eng. J. 354 (2018) 182–190, https://doi.org/10.1016/j.cej.2018.08.005.

[46] J.Y. Xue, F.L. Li, Z.Y. Zhao, C. Li, C.Y. Ni, H.W. Gu, P. Braunstein, X.Q. Huang, J. P. Lang, A hierarchically-assembled Fe-MoS$_2$/Ni$_3$S$_2$/nickel foam electrocatalyst for efficient water splitting, Dalton Trans. 48 (2019) 12186–12192, https://doi.org/10.1039/C9DT02201E.

[47] L.B. Xie, L.L. Wang, W.W. Zhao, S.J. Liu, W. Huang, Q. Zhao, WS$_2$ moiré superlattices derived from mechanical flexibility for hydrogen evolution reaction, Nat. Commun. 12 (2021) 5070, https://doi.org/10.1038/s41467-021-25381-1.

[48] Z.Z. Jiang, W.D. Zhou, A.J. Hong, M.M. Guo, X.F. Luo, C.L. Yuan, MoS$_2$ moiré superlattice for hydrogen evolution reaction, ACS Energy Lett. 4 (2019) 2830–2835, https://doi.org/10.1021/acsenergylett.9b02023.

[49] L.M. Deng, F. Hu, M.Y. Ma, S.C. Huang, Y.X. Xiong, H.Y. Chen, L.L. Li, S.J. Peng, Electronic modulation caused by interfacial Ni-O-M (M=Ru, Ir, Pd) bonding for accelerating hydrogen evolution kinetics, Angew. Chem. Int. Ed. 60 (2021) 22276–22282, https://doi.org/10.1002/anie.202110374.

[50] L. Huang, X. Zhang, G. Gao, H. Zhang, K. Rong, J. Chen, Y. Liu, X. Zhu, W. Wu, Y. Wang, J. Wang, S. Dong, Interfacial electron engineering of palladium and molybdenum carbide for highly efficient oxygen reduction, J. Am. Chem. Soc. 143 (2021) 6933–6941, https://doi.org/10.1021/jacs.1c00656.

[51] M.S. Hassan, P. Basera, S. Gahlawat, P.P. Ingole, S. Bhattacharya, S. Sapra, Understanding the efficient electrocatalytic activities of MoSe$_2$-Cu$_2$S nanoheterostructures, J. Mater. Chem. A 9 (2021) 9837–9848, https://doi.org/10.1039/D1TA01255J.

[52] Y. Huang, Y. Sun, X. Zheng, T. Aoki, B. Pattengale, J. Huang, X. He, W. Bian, S. Younan, N. Williams, J. Hu, J. Ge, N. Pu, X. Yan, X. Pan, L. Zhang, Y. Wei, J. Gu, Atomically engineering activation sites onto metallic 1T-MoS$_2$ catalysts for enhanced electrochemical hydrogen evolution, Nat. Commun. 10 (2019) 982, https://doi.org/10.1038/s41467-019-08877-9.

[53] B. Ruqia, S. Choi, Pt and Pt-Ni(OH)$_2$ electrodes for the hydrogen evolution reaction in alkaline electrolytes and their nanoscaled electrocatalysts, ChemSusChem 11 (2018) 2643–2653, https://doi.org/10.1002/cssc.201800781.

[54] Z. Zhang, L. Deng, Z. Zhao, Y. Zhao, J. Yang, J. Jiang, G. Huang, Y. Mei, Nickel nanograins anchored on a carbon framework for an efficient hydrogen evolution electrocatalyst and a flexible electrode, J. Mater. Chem. A 8 (2020) 3499–3508, https://doi.org/10.1039/C9TA13632K.